metals

MDPI

Article

Microstructural Evolution of Wrought-Nickel-Based Superalloy GH4169

Wei Zhou [1], Xiaohua Chen [2,*], Yanlin Wang [1], Kaixuan Chen [1], Yuzhi Zhu [1], Junwei Qin [1], Zidong Wang [1,*] and Lingli Zuo [3]

[1] School of Material Science and Engineering, University of Science and Technology Beijing, Beijing 100083, China
[2] State Key Laboratory for Advanced Metals and Materials, University of Science and Technology Beijing, Beijing 100083, China
[3] Beijing National Innovation Institute of Lightweight Ltd., Beijing 100083, China
* Correspondence: chenxh@skl.ustb.edu.cn (X.C.); wangzd@mater.ustb.edu.cn (Z.W.)

Abstract: To investigate the microstructural evolution of wrought-nickel-based superalloy GH4169 from the original ingot to the finished product of manufacturing processes, different kinds of etchants and etching methods were used to show the fine precipitates and their morphologies. The obtained microstructures can vary in size, type, distribution, location, formation, and interactions of multiple phases, which were observed and analyzed by optical microscopy (OM), scanning electron microscopy (SEM), and an energy dispersive spectrometer (EDS). The dendrite segregation behavior of as-cast superalloy GH4169 was investigated. In addition, the microstructural evolution mechanism of second-phase particles during dynamic recrystallization was analyzed. This work sheds light on the evolution of the second-phase structure of nickel-based superalloys during the preparation process, providing guidance for process development and visual interpretation of the relationships between microstructure and properties.

Keywords: superalloy; GH4169; microstructure; precipitates; homogenization; deformation

Citation: Zhou, W.; Chen, X.; Wang, Y.; Chen, K.; Zhu, Y.; Qin, J.; Wang, Z.; Zuo, L. Microstructural Evolution of Wrought-Nickel-Based Superalloy GH4169. *Metals* **2022**, *12*, 1936. https://doi.org/10.3390/met12111936

Academic Editor: Maciej Motyka

Received: 25 October 2022
Accepted: 9 November 2022
Published: 11 November 2022

1. Introduction

Nickel-based superalloy is an important class of materials that has developed rapidly [1,2]. GH4169 is a deformable one and the most widely used age-hardenable nickel-based superalloy. It has a good combination of advanatgeous mechanical properties, comprehensive strength, and good ductility over a broad temperature range [3,4]. The material was designed for aviation and aerospace power systems, land-based gas turbines, oil and gas fields [4,5], fuel cell applications, and as an alternative to high-quality stainless steel [6,7]. This alloy can be tailored to have unique sets of properties through control of its microstructure, including grain size and precipitate type, morphology, distribution location, quantity, and significant attributes, to obtain wrought superalloy materials suitable for specific service conditions [3–5]. The microstructure of wrought nickel-based superalloy GH4169 under various states can be obtained by various inspection and etching methods [8,9].

For GH4169, homogenization is a critical process after casting for the following plastic deformation (in particular, for forging). This plastic deformation always takes place at high temperatures, the main deformation mechanism of which is dynamic recrystallization (DRX) [8,10–12]. On the one hand, homogenization plays a mechanical crushing role to eliminate the primary coarse dendritic structure and improve the as-cast microstructure. On the other hand, hot forging results in simultaneous deformation and recrystallization, during which new grains re-nucleate and grow at the original coarse austenite grain boundaries, and second-phase particles, along with the grains, are refined [13,14]. The difference in grain growth rate between the dynamics of recrystallized grains and meta-dynamics of recrystallized grains is attributed mainly to the presence of the δ phase below

the δ solvus temperature, and to the differences in the characters of grain boundaries above the δ solvus temperature [11,14]. These main influencing mechanisms depend on the initial microstructure, chemical composition, and hot forming conditions (including deformation strain, deformation temperature, strain rate, cooling specification, etc.) [12]. Reasonable control of hot deformation parameters is vital for obtaining the microscopic grain structure that meets the requirements [10].

There are many kinds of inclusions in superalloys, including oxide inclusions (such as Al_2O_3, MgO, CaO, etc.), carbides, nitrides, sulfides, boride inclusions (such as TiC, TiN, CeS, MB_2, and M_3B_2), and composite inclusions consisting of two or more of the above-mentioned inclusions [15]. Several studies have shown that the amounts of nitrides and carbo-nitrides in alloys are the largest in the GH4169 alloy—one order of magnitude higher than that of oxide inclusions [16]. Inclusions are found to be the nucleation cores of primary carbides (MCs), and in this context, large inclusions often cause coarse carbides, which seriously deteriorate the mechanical properties, including the fatigue properties of the alloy [4]. Most of the large MCs with MgO-Al_2O_3 cores are uniformly dispersed in the matrix with different shapes, including irregular, island-like, or blocky [17]. MC and secondary carbides involving $M_{23}C_6$ and M_6C, where M stands for a combination of metallic elements Nb, Mo, Ti, Cr, Ta, or Hf, form in GH4169 [3]. The MCs are generally undesirable due to their detrimental effects on the mechanical properties [18]. Meanwhile, the secondary carbides uniformly dispersed along the grain boundaries can inhibit grain boundary sliding, and in consequence improve the strength [18] and prevent damage accumulation during high-temperature creep [4]. The composite inclusions in GH4169 exhibit a layered structure with MgO-Al_2O_3 as the core, NbC in the outer layer, and (Nb, Ti)(C, N) as the intermediate layer, which all nucleate sequentially above the liquidus temperature of the alloy [15,16]. Specifically, the formation temperatures of MgO-Al_2O_3 and TiN are about 1600 and 1450 °C, respectively. With a temperature below the melting temperature, two main segregation products, MC and Laves phase, are successively precipitated in the residual liquid phase enriched by solute. The precipitation temperature of MC is about 1252 °C, and the Laves phase is formed at the solidification end between 1186 to 1171 °C [9]. Carbides in superalloys have stability at high temperatures and are designed to improve high-temperature strength by strengthening grain bonding and preventing grain-boundary sliding. In addition, carbides cause crack initiation and propagation during plastic deformation [19,20]. Only an appropriate and reasonable carbide-size distribution can achieve a good combination of strength and plasticity [20]. Apart from the inclusions and carbonitrides, some nickel-based superalloys contain strengthening phases, such as γ″, γ′, and δ; and topologically closed-packed (TCP) phases, such as Laves, μ, and σ phases [4,21].

In this work, the microstructures of GH4169 superalloy was characterized in as-cast, homogenized, and hot-forged states. The formation and evolution mechanisms of microstructure were revealed. Specifically, the evolution of second-phase particles, especially the elimination of Laves phases and the refinement of MCs were evaluated. This work provides guidance for the design of homogenization and hot deformation.

2. Experiments and Methods

The superalloy GH4169 ingot was prepared by vacuum induction melting (VIM) with a diameter of 120 mm, taking a cylinder sample (Φ30 mm × 10 mm) at a mid-radius (R/2) of ingot, and its chemical composition was detected by a CX-9800 (L) (Wuxi Create Analytical Instrument Co., Ltd, Wuxi, China) vertical inductively coupled plasma optical emission spectrometer (ICP-OES). The compositions of the alloy are shown in Table 1.

Table 1. Chemical composition of as-cast superalloy GH4169 (wt %).

Position	C	Al	Co	Ti	Mo	Nb	Cr	Fe	Ni
R/2	0.037	0.541	0.850	0.966	2.978	5.561	17.989	18.077	Balance

The homogenized (1160 °C × 24 h + 1200 °C × 24 h) samples were forged at the temperature of 1050 °C with 10% and 80% reductions, respectively. The homogenization and the hot forging temperatures/times were chosen based on the DSC results and literature [8,10,11,14,22,23]. All other samples for microstructure analysis were performed in 10 mm × 10 mm × 5 mm squares by wire cut electrical discharge machining (WEDM) (Taizhou Ruite Machinery Equipment Co., Ltd., Taizhou, China), and the samples were sequentially ground with 400# to 2000# metallographic sandpaper to remove the oxidized surface layer. Each stage of fine grinding should remove the scratches left by the previous process, then one uses a soft plush cloth for mechanical polishing. Finally, ultrasonic vibration cleaning was carried out in an ethanol solution.

Non-metallic inclusions and MCs can be best observed in the as-polished condition without etching. The etching morphology of superalloys can vary greatly depending on the condition of the material and requires different etching methods. Even the same as-cast specimen will obtain different microstructures using different etching methods. Numerous etchants are used to reveal the structures of superalloys. Table 2 lists some of the most commonly used etchants. We polished the sample surface with a diamond slurry (1 μm or finer) before etching. The metal surface has to be etched as soon it is polished, cleaned, and dried without any delay. The periphery, R/2, and center of the ingot are presented herein, showing the use of different etchants as functions of alloy composition segregation, heat treatment, and microstructural phases. Since the statistical grain size must not contain twinned regions within it or sub-grains, etchants 3 and 4 were used to minimize the appearance of twinning [22].

Table 2. Types and etching methods of etchants for superalloy GH4169.

Etchant No.	Etchant Name and Composition	Etching Method	Experimental Parameters
1 [24]	Saturated oxalic acid solution: 15 g oxalic acid + 100 mL H_2O	Electrolytic Etching	Constant current: 50 mA, 10~15 s
2 [21,25]	Kalling′s II Reagent: 1 g $CuCl_2$ + 20 mlHCl + 20 mL C_2H_5OH	Immerse or swab	As-cast: 5~15 s Homogenization: 30~40 s
3 [26]	20%H_2SO_4 + 80%CH_3OH	Electrolytic polishing	Constant current: 2A, 4~6 s
4 [9,22,26]	15 g CrO_3 + 10 mL H_2SO_4 + 150 mL H_3PO_4	Electrolytic Etching	Constant current: 50 Ma, 6~10 s
5 [22]	1 g $KMnO_4$ + 5 ml H_2SO_4 + 60 mL H_2O + 0.2 ml HCl	Boiled and immerse	1~7 min
6	Saturated oxalic acid solution: 15 g oxalic acid + 100 mL H_2O	Boiled and immerse	1~2 min, cleaning the surface oxide

The sample must be polished surface before etching.

The microstructure, including element segregation, and precipitated phases of GH4169 ingot were observed by OM and SEM (InLens mode 5 kV, Carl Zeiss, Oberkochen, Germany), and the average grain size of the alloy was determined by the quantitative metallographic intercept method. The average grain size and particle size measurements from the light microscope were calculated using Image J software (1.53e, National Institute of Mental Health, Bethesda, MD, USA) with an accuracy of 0.2 microns. The morphology observation and micro-area composition analysis of the material surface can be carried out simultaneously by EDS with an acceleration voltage of 20 kV; and the geometric morphology, particle size, particle size distribution, and phase structure of intermetallic compounds precipitated from the material were statistically analyzed.

The electron probe microanalyzer (EPMA) was applied to accurately analyze light elements such as C on a Shimadzu Model EPMA-8050G (Shimadzu Corporation, Kyoto, Japan) at an accelerated voltage (Acc V) of 15 kV and beam current (BC) of 20 nA. Differential scanning calorimetry (DSC) analysis was performed with the NETZSCH STA 449 F5 Jupiter synchronous thermal analyzer (NETZSCH-Gerätebau GmbH, Selb, Germany), and the sample was sectioned from R/2 of the ingot and processed into a small cylindrical shape

5 mm in diameter and 2 mm in length; the surface was ground and ultrasonic cleaning with ethanol, and then weighed (158.1 mg). During the experiments, the DSC furnace temperature was raised from 30 to 1400 °C with a rate of 10 °C/min, using argon with a flow rate of 70 mL/min as inert protection and a Pt crucible with an Al_2O_3 lining. The temperature was kept at 1400 °C for 20 min and then cooled naturally.

3. Results

3.1. Cast Microstructure

As shown in Figure 1a, examining the polished surface carefully before etching is a good way to find and predict the phase types of inclusions (red arrow indication) and MCs (black arrow indication). Some minor second-phase particles such as dot inclusions and blocky MCs could be easily observed in the as-polished condition using bright field illumination by OM. Many details can be observed more clearly, such as the white arrow pointing to the Laves phase hidden in the background of the picture. Figure 1b shows the histogram and cumulative frequency distribution of 520 inclusions and MCs particles. The average particle size was 3.0 μm, 90% of particles were below 4.6 μm but above 2.4 μm, and 50% of particles were 2.4 μm or less.

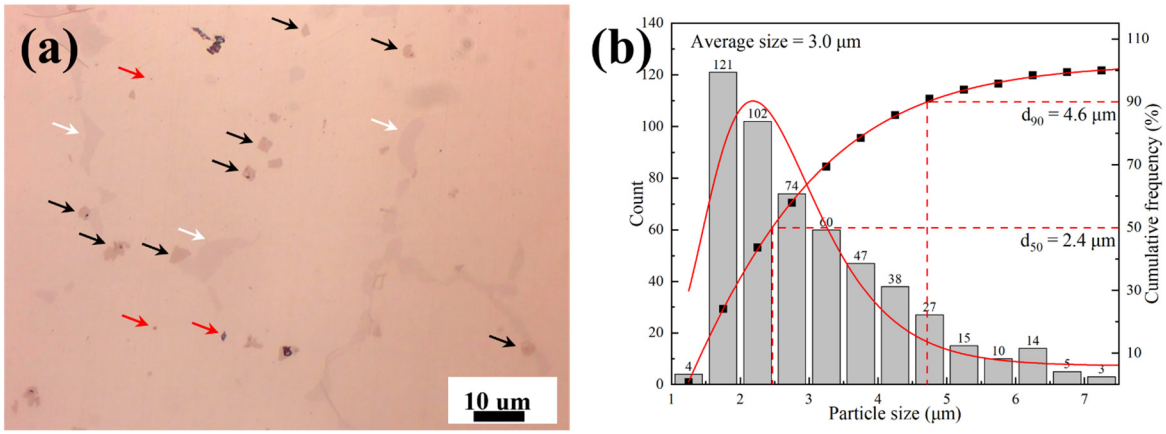

Figure 1. (**a**) OM image of as-cast GH4169 at R/2, unetched (red arrow pointing to inclusion, the black arrow pointing to MC, the white arrow pointing to the Laves phase); (**b**) histogram and cumulative frequency distribution of particle sizes at R/2 of the ingot.

The as-cast microstructure was observed under OM by electrolytic etching. In Figure 2a, the inclusions are all orange and randomly scattered in the γ-matrix, and a large number of grey block MCs are randomly distributed along grain boundaries. A Laves phase formed in the inter-dendritic regions during solidification. Figure 2b shows the morphology and distribution of Laves phases, MCs, and inclusions enlarged. The white arrows point to the island Laves phase with rounded and smooth edges. The black solid arrows point to MCs as nucleation cores with inclusions and MCs with an amorphous core are identified by black dashed arrows. The red dashed frame shows the presence of needle-like phases around the Laves phase and the eutectic phase.

The liquid in contact with the mold wall solidifies relatively rapidly, and the surface of the ingot forms a fine equiaxed grain structure, as shown in Figure 3a. The grains then start to grow towards the center, in the general direction of maximum heat flow, giving a columnar grain structure, as shown in Figure 3b. The directional growth of the columnar dendrite region is about 10 mm. Columnar-to-equiaxed transition occurs when the equiaxed grains are sufficiently large in size and number to impede the advance of the columnar front. The remaining structure forms coarse-equiaxed grains as solidification progresses towards the center, as shown in Figure 3c. The segregation of elements at R/2 is shown in Figure 3c. Fe, Cr, and Mo elements in superalloy GH4169 are mainly dissolved in the austenitic γ-matrix, which plays a solid solution-strengthening role. With

the addition of Nb, Mo, Al, Ti, and other elements, ordered intermetallic and carbonitrides form extremely effective precipitation-strengthening second phases through a series of heat treatment and hot deformation processes. According to the EDS-mapping analysis of compositions and the obvious dendritic morphology in Figure 3, most of the elements had serious dendritic segregation in the ingot, and the positive-segregation elements Nb, Mo, and Ti tended to be enriched in inter-dendritic regions. The negative-segregation elements Fe, Cr, and Ni were more likely to be enriched in the dendrite core [4,22]. Due to the extremely low content of Ti element, only sporadic, non-obvious segregation points can be seen in the figure. The overall distribution of Al element is relatively stable.

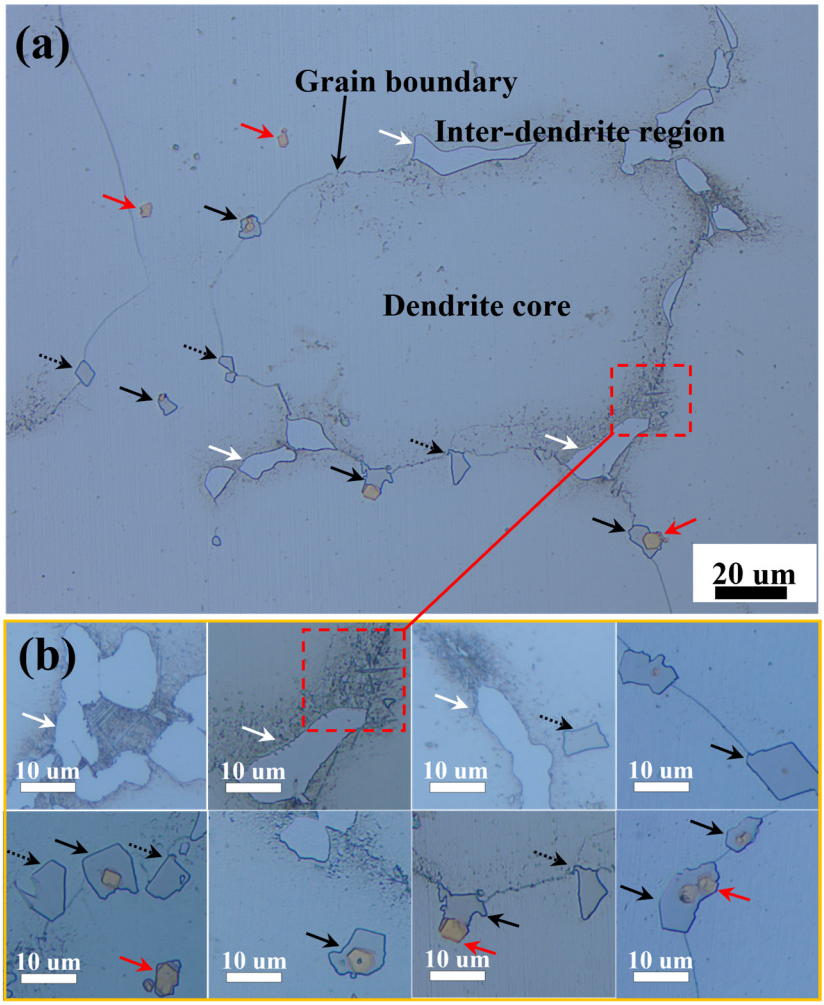

Figure 2. Microstructure of the second phases at R/2 of as-cast GH4169 with etchant 1 by OM, (**a**) R/2 500×, (**b**) partially enlarged pictures of second phases (red arrow pointing to orange inclusion, the black arrow pointing to MC, the white arrow pointing to Laves phase).

The structure, morphology, and composition of MCs are shown in Figure 4, according to the SEM-mapping distributions of the main elements combined with EDS-point scanning analysis. Figure 4a shows the major phases present in as-cast GH4169, and the compositions of the γ-matrix (Point A) and Laves phase (Point B) measured by EDS in Table 3. The Laves phase is a low-dissolving-point, brittle intermetallic compound, which is aggregated and distributed in the form of islands [3,4,21,27,28]. Figure 4a,b show the three types of MCs, a typical composite structure of dark inclusions, and gray MCs in superalloys (Figure 4a) that look like a cluster block or octahedron. From the compositional SEM mapping of inclusions and MCs, it can be seen that there were three layers in total. TiN nucleated on fine Al_2O_3; and the periphery of TiN contained very little Ti or N, and MC grew with TiN

as the nucleus. From the SEM-mapping of elemental distribution in Figure 4b, it can be seen that the other two MCs were (Nb, Mo)C without oxide inclusion as the core and (Nb, Mo, Ti)C with only TiN as the core, respectively. The above research results show that the formation of MC and TiN includes two stages: nucleation and growth, and the nucleation methods include homogeneous nucleation and heterogeneous nucleation. Heterogeneous nucleation was carried out utilizing the existing Al_2O_3, TiN, and other inclusion impurities in the alloy liquid, as shown in Figure 4. Homogeneous nucleation relies on its own energy fluctuations and structural fluctuations for nucleation, so there is no oxide core.

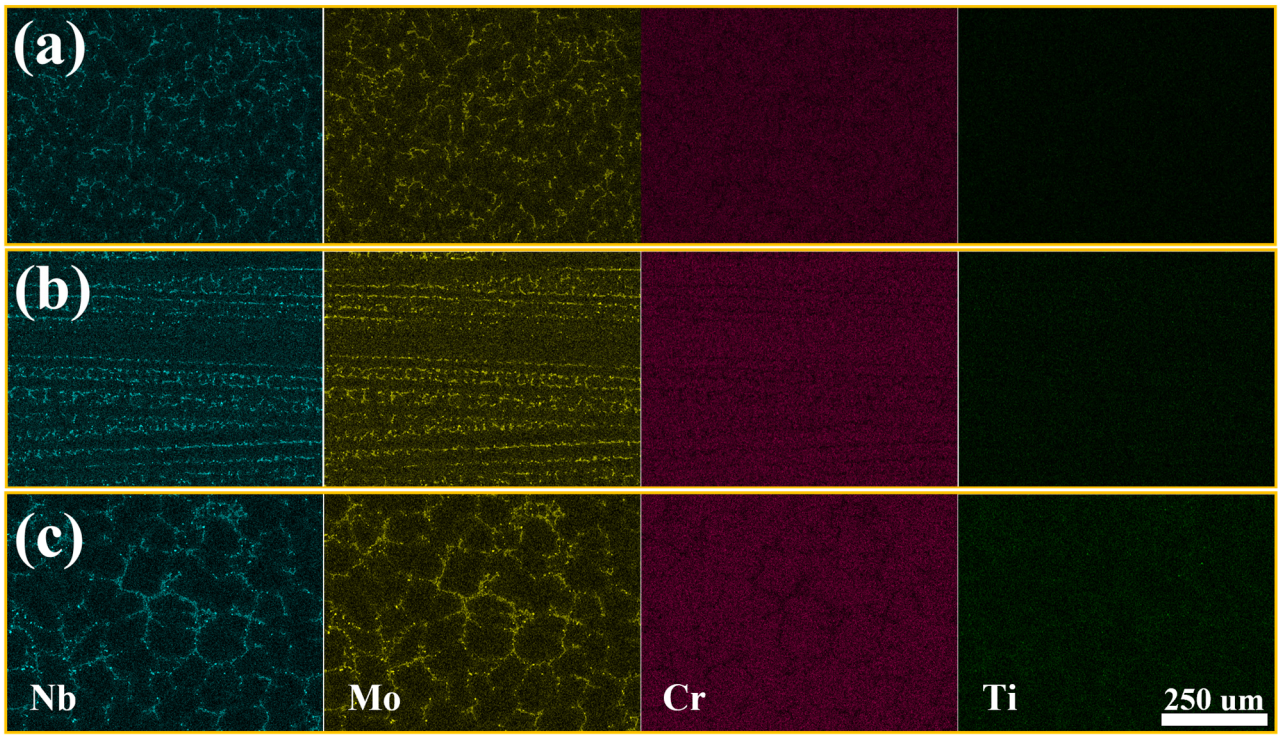

Figure 3. SEM-mapping micrographs showing the distributions of segregated elements in different positions of an ingot with etchant 2, (**a**) surface, (**b**) periphery, (**c**) R/2.

Table 3 lists the types of precipitated phases and their chemical components in the dendrite core/inter-dendritic regions (marked in Figure 4a), according to the EDS-point scanning results.

Moreover, in order to make clearer the carbon content in the shell phase encapsulated by the core phases in Figure 4, EPMA results are presented in Figure 5 and Table 4. The shell phase (point 5 in Figure 5) encapsulated the core phases (points 1~4 in Figure 5) and exhibited 42.537 at% C, along with 29.326 at% Nb, which strengthens the conclusion that these shell phases were carbides. The chemical compositions measured at the points labeled 1 to 5 in Figure 5 are reported in Table 4. The most typical multilayer composite structure of MCs can be observed clearly in Figure 5, surrounded by a large number of acicular precipitated phases with thicknesses of less than 100 nm.

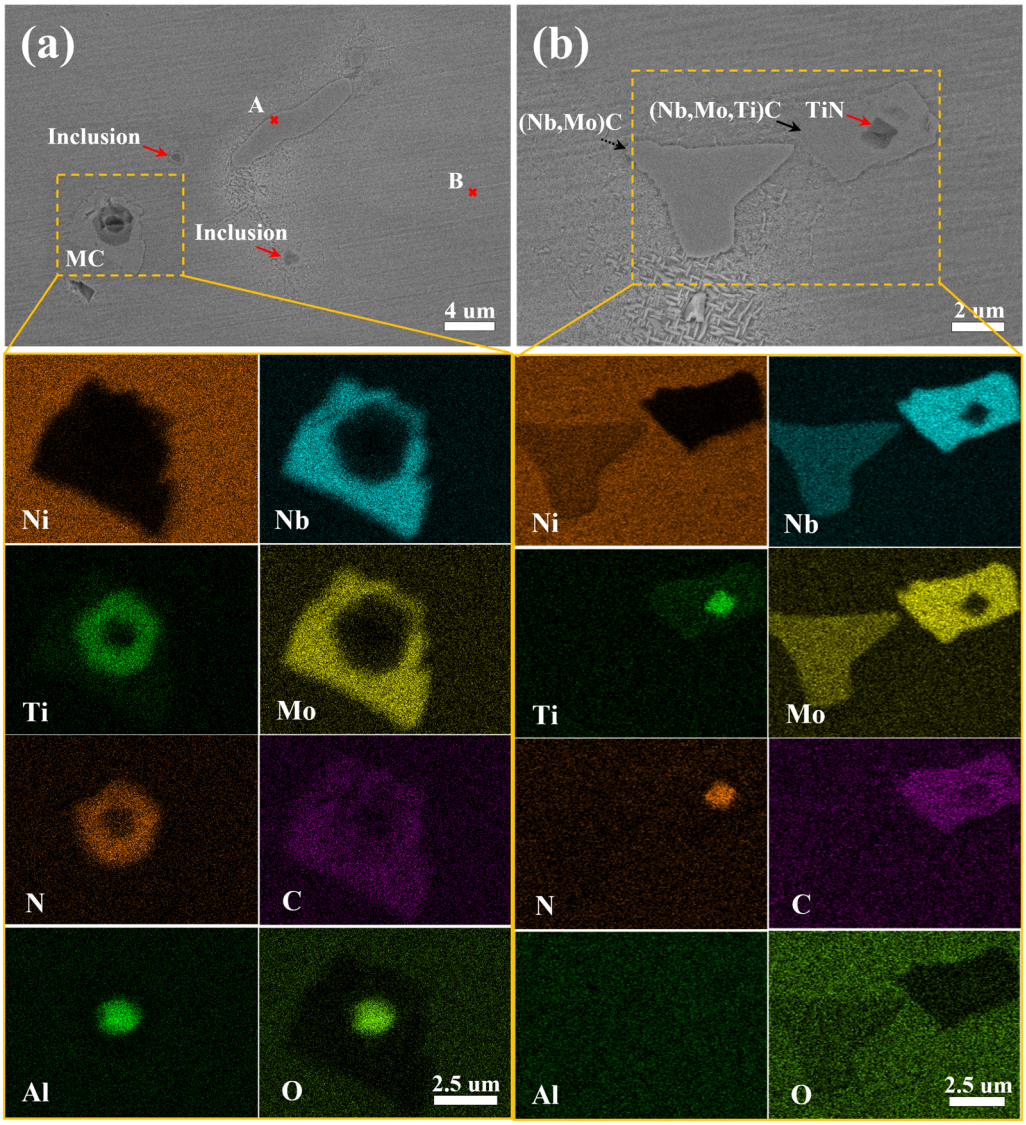

Figure 4. SEM-mapping micrographs and EDS-point analysis results of as-cast GH4169 with etchant 1. (**a**) Distribution of segregation structure. (**b**) Typical composite structures of inclusions and MC.

Table 3. Composition analysis and phase identification in Figure 4a measured by EDS point (wt%).

Point	Ni	Cr	Fe	Al	Ti	Mo	Nb	Phase
A	52.90	19.78	18.95	0.70	0.88	3.12	3.67	γ-matrix
B	40.10	11.50	10.20	0.55	1.17	7.54	28.95	Laves

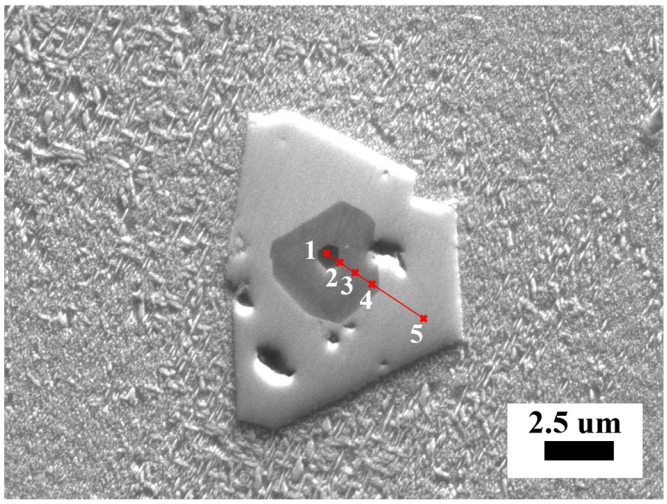

Figure 5. The morphologies and compositions of MCs were measured by EPMA-8050G (Acc V: 15.0 kV/BC: 19.4 nA). EPMA analysis of the chemical compositions of points 1 to 5.

Table 4. The EPMA results of points number 1 to 5 are shown in Figure 5 (at%).

No.	Ni	Cr	Fe	Al	O	Ti	N	Mo	Nb	C
1	0.221	0.109	0.076	9.669	73.867	8.871	5.231	0	0.56	1.396
2	0.471	0.349	0.19	1.181	22.351	30.03	40.678	0	2.382	2.368
3	0.432	0.296	0.167	1.509	37.14	24.77	30.847	0	1.625	3.214
4	1.602	0.782	0.46	0.042	7.58	32.003	48.872	0	2.928	5.731
5	8.87	2.92	2.908	0.184	6.984	6.272	0	0	29.326	42.537

Regarding the image brightness and phase contrast of the microconstituents, Figure 6a shows the typical microstructure of the inter-dendritic region, where the gray blank area is the dendrite core area, and the white area is the inter-dendritic area accompanied by a large number of island and block phases, the formation of Nb-rich precipitates such as Laves phases, and MCs in the inter-dendritic region. Figure 6b–e show the amplification of the microstructure in the red dotted frame. It can be observed that the precipitates were mainly distributed in the inter-dendritic region, and the precipitates at different positions were quite different. As shown in Figure 6b,d, long needle-like δ phases appeared at the junction of the black island-like Laves phases, and multiple elongated needle-like δ phases were superimposed on the grain boundaries in Figure 6h. The δ phases were mainly distributed along the grain boundaries and were granular. As shown in Figure 6e, there were plate-shaped δ phases at the grain boundaries, which can inhibit grain boundary sliding and improve durability.

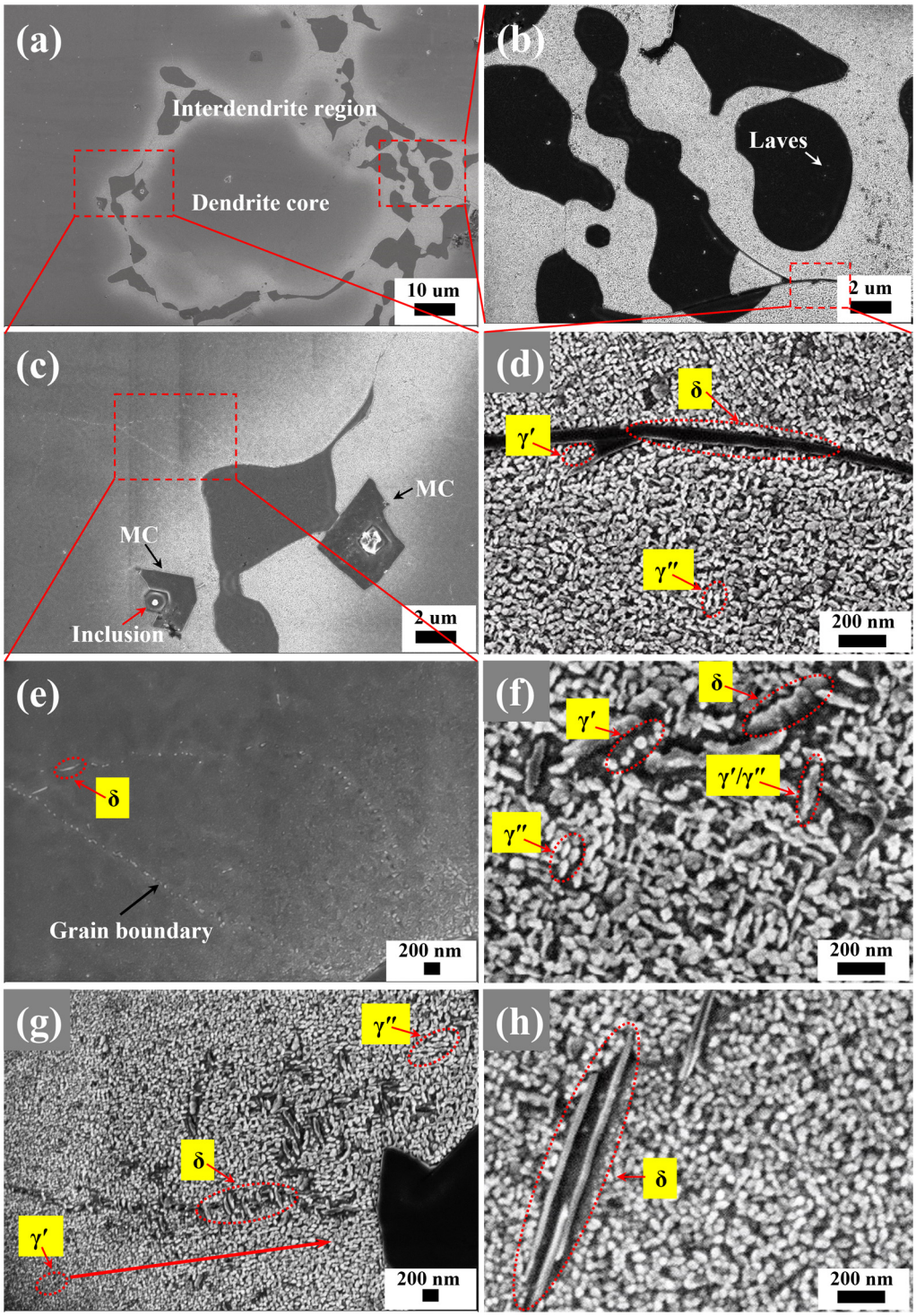

Figure 6. Morphologies of the most important precipitates of as-cast GH4169 with etchant 3 and 4 by SEM. (**a**) Microstructure of dendritic segregation. (**b**) Island-like Laves phase. (**c**) MC and Laves phases. (**d**) Long needle-like δ. (**e**) Plate-shaped δ precipitates at grain boundaries. (**f**) Finely dispersed mixture of γ″(ellipsoidal [3,5,29,30]), γ′(spherical [3,4,29,30]), γ′/γ″(co-precipitated composite [30,31]), and δ (plate-shaped [3,5,26]), precipitates. (**g**) Change trend of precipitates with Nb content increasing. (**h**) Fine needle-like δ. The phase types of the fine γ″, γ′, γ′/γ″, and δ precipitates are predicted based on their reported features in the literature [3–5,18,26,29–32].

Under higher magnification, short rod-like or plate-shaped δ precipitates can be observed in Figure 6f–h, spherical γ′ precipitates with diameters of 20 to 50 nm, usu-

ally present in Nb-poor regions or hidden between other precipitates. The typical disc-shaped/ellipsoidal γ″ had a diameter of 60 to 120 nm and a thickness of 5 to 20 nm, and looked like a rice grain when observed under the SEM at 20,000 magnification. Corresponding regions with reduced Nb content had lower precipitation potential. It was observed that the γ″ particles were with more numerous as precipitate size increased; a large number of spherical γ′ particles are attached to the surface in Figure 6f. The red arrow in Figure 6g points to the direction of the gradual increase in Nb content, and it is obvious that the precipitation phase is gradually coarsening. Precipitation of the spherical γ′ particles does not appear to precede that of the ellipsoidal γ″ particles [29]. Several different fault configurations were identified for the co-precipitated composite γ′/γ″ particles and γ″/γ′/γ″ co-precipitates. Multiple deformation mechanisms can operate at the same time, leading to the development of different composite precipitate morphologies [26,30–32].

3.2. DSC Analysis

When the ingot is heated to 100 to 200 °C below the solidus line, if there is a low dissolving point segregation phase, it needs to be lower than its initial dissolving temperature, and it needs to be kept at this temperature for a long time to make the solute atoms fully diffuse, which can reduce or eliminate micro-segregation. This is particularly important for wrought products, which should be homogenized to avoid the carrying over of the Laves phase. As shown in Figure 7, in the change curve of DSC with the increase in temperature, the endothermic peaks generated by the dissolving process of Laves phase, MCs, and γ-matrix appear successively, and the peak temperatures are T^{Laves}_{peak} = 1199.6 °C, T^{MC}_{peak} = 1274.7 °C, and T^{γ}_{peak} = 1332.6 °C, respectively. The peaks of MC and γ-matrix overlap and superimpose together, and the inflection point is the peak point of MC. Since the solid phase baseline and the liquid phase baseline are not on the same horizontal line, this will cause a certain deviation in the data. The dotted red line was connected at the beginning of the endothermic reaction and the end of the endothermic reaction of the sample, and tangent lines were drawn from the peak point to the left side of the peak. The initial dissolving temperature of Laves phase was T^{Laves}_{onset} = 1178 °C, the initial dissolving temperature of MC was T^{MC}_{onset} = 1233.7 °C, and the initial dissolving temperature of γ-matrix was T^{γ}_{onset} = 1280 °C. As the γ-matrix is the main body of superalloy GH4169, the initial dissolving temperature (T^{γ}_{onset}) corresponds to the solidus temperature of the alloy in the melting process, the end temperature T^{γ}_{offset} = 1345 °C corresponds to the liquidus temperature of the alloy, and the T^{γ}_{peak} is the melting point (T_m) of the alloy.

3.3. Homogenization Microstructure

Homogenization is a heat treatment method for as-cast superalloy at high temperatures that takes a long time to remove the low melting phase and microscopic segregation, so homogenization is a diffusion-controlled homogenization temperature process. According to the DSC test data, the holding temperature of homogenization heat treatment was set to 1160 °C for 24 h first and then 1200 °C for 24 h, just below the initial dissolving temperature of the Laves phase and MC. The determination of holding time refers to the relevant references [14,21,23]. Figure 8 shows the microstructure after the homogenization treatment. By comparing it with the as-cast results, most of the second phases (in particular the inter-dendritic Laves phase) were dissolved in the homogenized state, and only a small amount of MCs remained in the matrix. The result indicates a good effect of the homogenization process applied in this work on improving the as-cast microstructure.

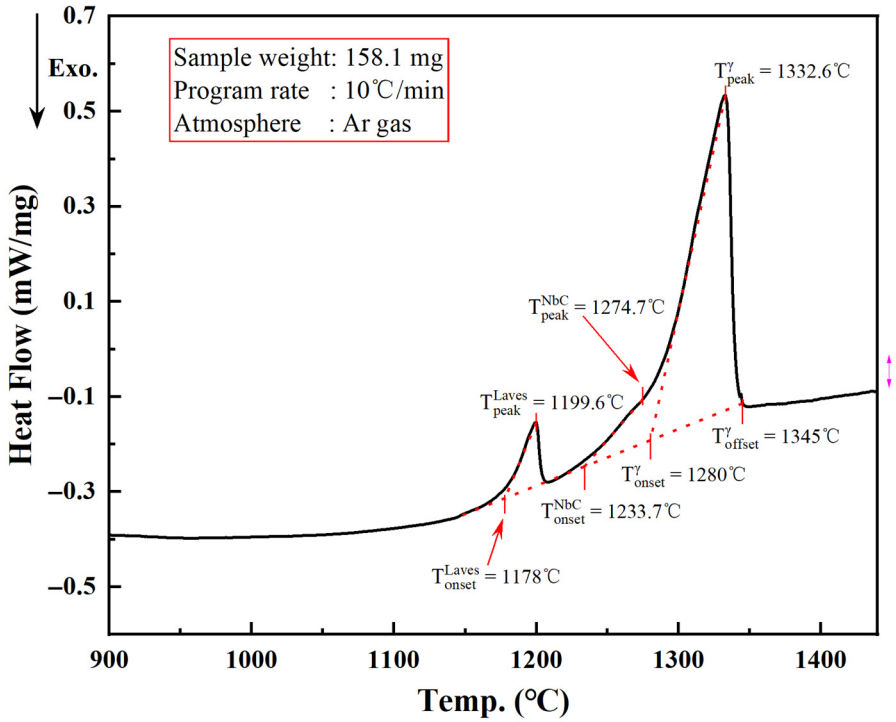

Figure 7. Thermal analysis curve of as-cast GH4169 DSC.

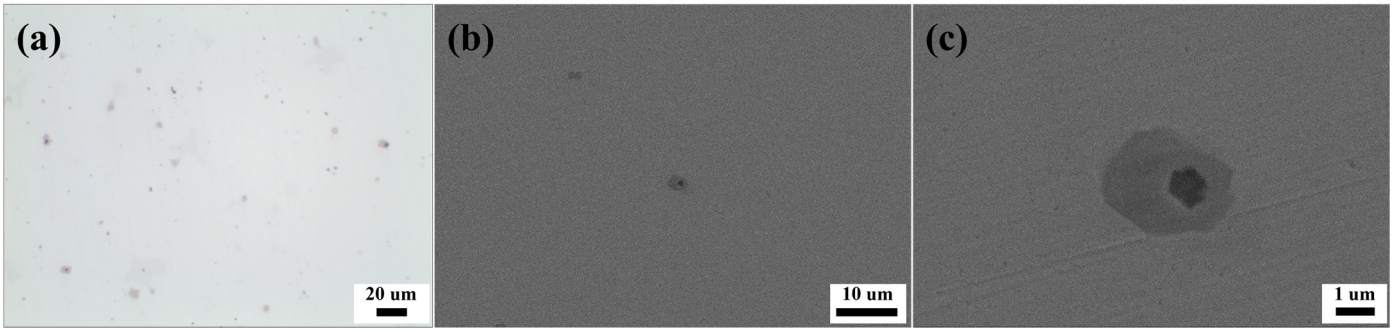

Figure 8. Microstructural evolution during homogenization treatment. (**a**) OM image 500×, (**b**) SEM image 5KX, and (**c**) SEM image 32KX.

3.4. Forging Microstructure

The microstructure of specimens after forging at 1050 °C with a 10% reduction was a partially recrystallized grain structure, as presented in Figure 9a–c, which reveals a "necklace"-type duplex grain structure surrounding second-phase particles/precipitates and grain boundaries. When the deformation is small, the stress–strain mismatch will result in a mixed grain structure [8,11,14,22]. Figure 9a clearly shows that the nucleation sites for the recrystallized grains were prior grain boundaries, and the new grains originated at the old grain boundaries. As the strain during the deformation progressed, the dislocation density of the new grains increased, which reduced the driving force for their further growth. Figure 9b,c show that the first recrystallized nuclei appeared in the vicinity of the large particles. During the deformation process, the larger particles were fully broken into small particles, and it is difficult for harder particles to deform. Dislocations accumulatde near the particles, resulting in large distortion of the surrounding γ-matrix and forming a high-density substructure that is prone to nucleation, which is well known as the DRX mechanism of particle stimulated nucleation (PSN). Fine recrystallized grains along the grain boundary can be obtained at high temperatures via PSN stimulated by adequate storage energy, which was provided by large deformation near coarse second phases, such

as MCs and inclusions [33]. The nucleation of DRX mainly occurred at the primary grain boundaries and the recrystallization grain boundaries, and other parts of the nucleation of DRX occurred near the second-phase particles [34]. The large-angle grain boundary formed by continuous dynamic recrystallization (CDRX) is a necessary condition for discontinuous dynamic recrystallization (DDRX) to form recrystallized grain nucleation. DDRX may also occur at or near other heterogeneous sites, such as shear bands and kink bands, but these sites are more frequently produced at low deformation temperatures or high strain rates [24].

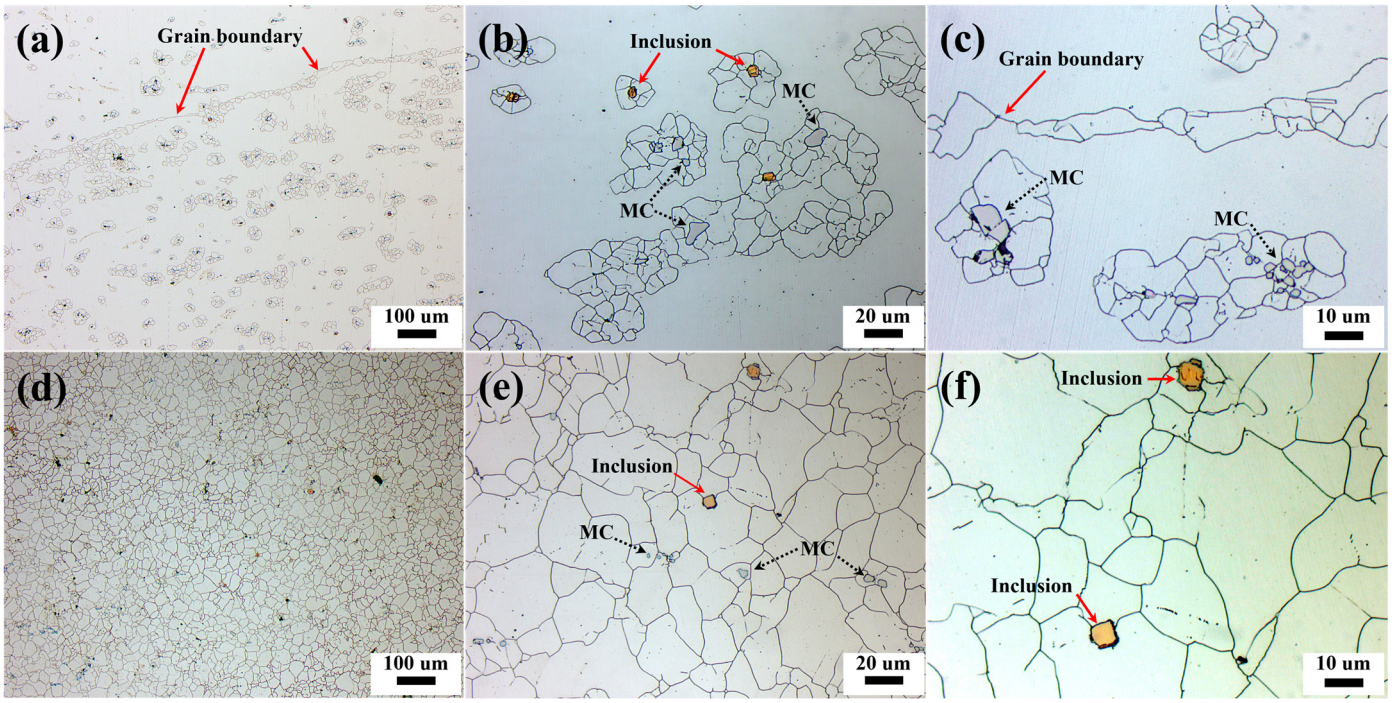

Figure 9. Untwinned grains of as-forged GH4169 by OM after etching with etchants 3 and 4: 10% deformation: (**a**) 100×, (**b**) 500×, (**c**) 1000×; 80% deformation: (**d**) 100×, (**e**) 500×, (**f**) 1000×.

After forging at 1050 °C with 80% reduction, it became a new nucleation center and fully dynamic recrystallization occurred. Figure 9d–f displays a "fine" equiaxed grain structure with an average size of 16.8 μm. Large pieces of gray MCs were completely broken and scattered inside the grains, and a small number of orange inclusions were distributed along the grain boundaries. Figure 9a shows a schematic representation of the necklace structure which was composed of fine equiaxed recrystallized grains. The nucleation mechanism of DRX in the alloy mainly initiates by strain-induced bulging of original grain boundaries, accompanied by twinning, and the sub-grain rotation near the grain boundary plays an auxiliary role; that is, the DRX grains first arch out and nucleate at the previous grain boundaries, forming necklace structures.

In forged alloy materials, the crack growth is mainly through carbides, and aggregated or large-sized carbides lead to long cracks. When the carbides and inclusions are completely broken and the size reaches a certain order of magnitude, the heterogeneous nucleation of the DRX will be promoted, and the grains will be rapidly refined (Figure 10). Figure 10a–c shows the partially recrystallized microstructure with 10% deformation, and Figure 10d–f shows the fully DRX microstructure with 80% deformation. Due to the small inclusions, no crack propagation was found, and the inclusions were well fused with the matrix (Figure 10e). As shown in Figure 10c,f, due to the largeness of some carbides and their weak bonding with the γ-matrix, the uneven deformation could not be completely broken, resulting in the fracturing of brittle inclusions on the surface or small cracks being formed at the interface. Most of the crack initiations were generated around particles with larger

than 4 μm. The larger the size of the particles, the more prone to fracturing. If the geometric essential dislocation density is high, deformation and strain localization will appear near the MCs; and inclusions after fatigue cyclic loading, crack initiation, and propagation will be caused. During the service life of the material, these MCs will become cracks. Microcracks mainly initiate and propagate at the interfaces between large MCs and the γ-matrix. Reducing the numbers of MCs and inclusions and making them smaller than 2 μm, along with appropriately adjusting the shape of carbides, can slow down the initiation and propagation of microcracks.

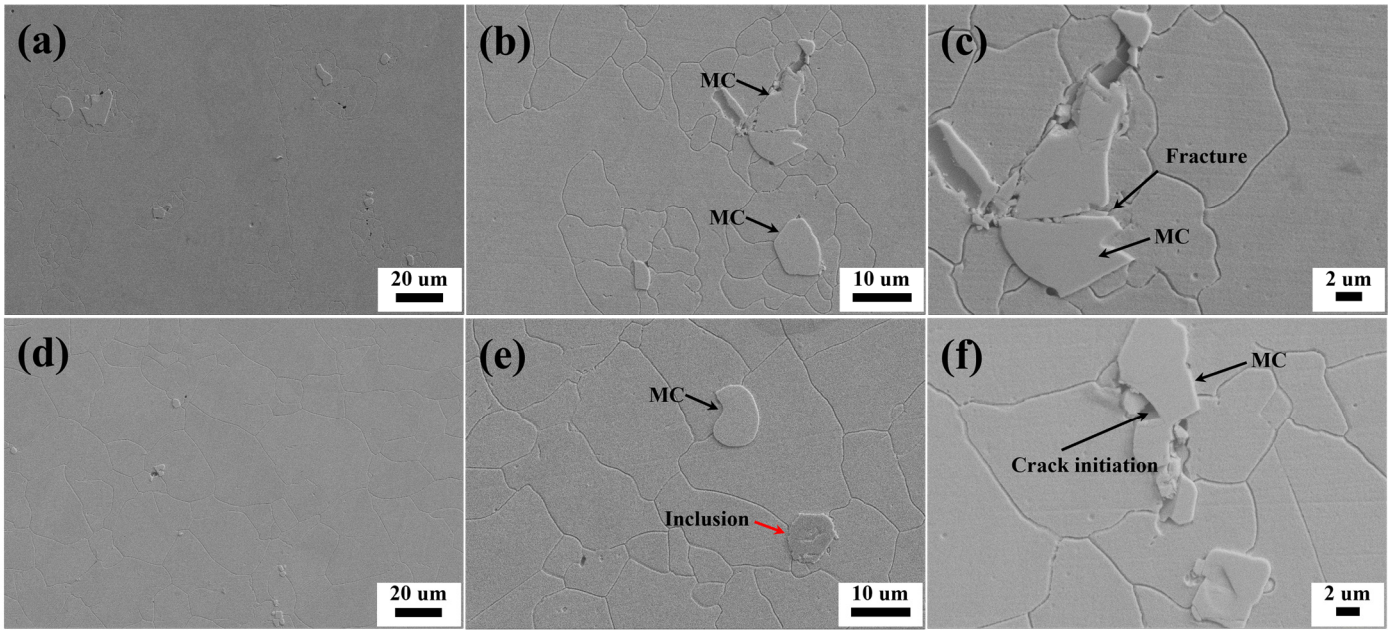

Figure 10. SEM micrographs of as-forged GH4169 with etchants 3 and 4. Partial recrystallization: (**a**) More carbides 2KX. (**b**) Lots of grain boundaries around MC 5KX. (**c**) Cracked carbides 11KX. Fully DRX: (**d**) Fewer carbides 2KX. (**e**) Homogeneous nucleation 5KX. (**f**) Crack initiation 10KX.

4. Discussion

In general, inclusions and carbides are necessary but not sufficient conditions for crack initiation and propagation in wrought superalloys [16,19,20]. Note that 76% of carbides were less than 3 μm, and those between 0.5 and 3 μm were not cracked [35]. The size distribution of MCs can be used to monitor the cooling rate in GH4169 ingots, provided that the same composition is taken into account [27]. The melting process reduces the contents of O and N in the melt, reduces the number and particle size of inclusions, and refines them into the micro–nano scale to reduce the number of large MCs [28]. In this research, the average particle size of inclusions and MCs was 3.0 μm, 90% of particles were below 4.6 μm in diameter, and Ti-rich inclusions appeared orange in color. Nb-rich MCs were grey. Most of the crack initiations took place around particles larger than 4 μm in as-forged GH4169. These large, blocky carbides can act as crack initiation sites, reducing fatigue performance. It is noted that the second phases of different sizes and compositions had major influences on the high-temperature mechanical properties [36]. Thus, it is vital to tailor the particle features in GH4169 for its excellent high-temperature performance.

The alloy ingot was treated by a two-stage homogenization heat treatment. The purpose was that the first stage of homogenization heat treatment temperature cannot exceed the initial dissolving temperature of the Laves phase, T^{γ}_{onset}, so that the temperature was maintained for a long time to completely dissolve all the segregated phases into the γ-matrix. The second stage of homogenization makes the metallic elements (Nb, Mo, Ti) diffuse into the solid solution matrix as fully as possible, making the composition more uniform, and eliminating composition segregation and dendritic segregation without

overheating. Therefore, the temperature cannot exceed the initial dissolving temperature of the MC, so that the MC's size is reduced and the hot working plasticity is improved. Considering the influence of the temperature difference in the heat treatment furnace, the homogenization temperatures of the first and second stages were 20–30 °C lower than the Laves phase and MC incipient dissolving temperatures, respectively. According to the references [14,21,23,28], the Laves phase can be eliminated or redissolved after homogenization at 1160 °C × 24 h + 1200 °C × 24 h, suggesting it was the most suitable homogenization process.

DRX is the most important grain refinement mechanism during the hot deformation of austenitic superalloys affecting the final microstructure, and hence the mechanical properties [37,38]. As the number of deformations increases, when DRX forms multilayer recrystallized grains, CDRX will be elongated along the grain boundaries and stimulated by PSN. The original grains are divided and new high-angle grain boundaries are formed so that DDRX can continue to develop to form equiaxed grains with an average grain size of 16.8 μm. The DDRX is the major deformation mechanism for the studied superalloy, and the rotation of the subgrain is a minor nucleation mechanism of DRX [12,24]. The cogging of the ingot requires a large amount of deformation, and the deformation direction changes alternately so that the as-cast structure can be fully broken, especially in the center position, where large MCs and inclusions are broken and bridged. In addition, some other studies indicate that it is possible to stabilize nanostructures at high temperatures through grain-boundary alloying, including grain-boundary segregation and its energetic competition with the formation of second phases [39].

In this study, the types and nucleation mechanisms of inclusions and MCs in the microstructure of as-cast superalloy GH4169 were analyzed. The numbers of inclusions and MCs can be controlled by controlling the contents of carbon, nitrogen, and oxygen elements in the melt. The MC has a high dissolving point, and the initial dissolving temperature can be as high as 1233.7 °C. It is difficult to refine by heat treatment. It is only broken by hot deformation. At the same time, new grains originate from the old grain boundaries, along with second phases, such as MCs and inclusions stimulated by PSN. Whether the material itself is plastically deformed, machined, or used in different environments, the formation and propagation of microcracks in superalloy GH4169 are related to the morphologies and sizes of second phases, such as MCs and nitrides. By reducing the number of these second phases and reaching their critical size, the microstructure of the alloy can be optimized, thereby improving the plasticity and toughness of the superalloy GH4169.

5. Conclusions

This study focused on accurate phase identification and characterization, which are vital to the success and quality control of these materials. The following conclusions were reached.

(1) The experiments illustrated the sizes, structures, and compositions of three typical MCs in as-cast superalloy GH4169, including homogeneous nucleation and heterogeneous nucleation mechanisms. The average particle size of inclusions and MCs was 3.0 μm, 90% of particles were below 4.6 μm in diameter, and 50% of particles were 2.4 μm or less in diameter. It is very effective at highlighting structural features such as second phases, consisting of Laves phases and MCs, in the inter-dendritic region; fine γ' precipitates and γ-matrix in the dendrite core region; and a large number of δ and γ'' precipitates between the two regions.

(2) According to DSC analysis, the suitable homogenization temperatures of the first and second stages are 20–30 °C lower than Laves phase and MC incipient dissolving temperatures; a reasonable two-stage homogenization process at 1160 °C × 24 h + 1200 °C × 24 h can eliminate the typical dendritic solidification structure.

(3) During the forging process of GH4169, the formation mechanisms of DRX are mainly DDRX and PSN, and nucleation mainly occurs at the interface of high-angle grain boundaries or critical-size second-phase particles. In forged materials, it was found that

crack initiation mainly occurs around MCs with particle sizes larger than 4 μm, and even fracturing occurs. The second-phase particles with a size of less than 2 μm become the center of the heterogeneous nucleation of DRX, and a large number of fine grains are generated around them.

This work provides an explanation of the inter-relationships between microstructure and processing of the superalloy GH4169, which is beneficial for solving the problems that arise during plastic processing, heat treatment, and long-term service.

Author Contributions: W.Z. conceptualization, investigation, and writing of the manuscript; Z.W. supervision and reviewing; X.C. and L.Z. resources and data curation; Y.W. correcting of the manuscript; K.C. funding acquisition; Y.Z. methodology and arranging illustrations; J.Q. software. All authors have read and agreed to the published version of the manuscript.

Funding: This work was supported by the Open Foundation of State Key Laboratory for Young Teachers of USTB (Fundamental Research Funds for the Central Universities, number FRF-IDRY-20-034), National Natural Science Foundation of China (grant number 52101119), the Beijing Municipal Natural Science Foundation (number 2214072), Advanced Metals and Materials (University of Science and Technology Beijing, number 2022-Z01), the National Natural Science Foundation of China (52071012 and 51971031), the Academic and Technical Leaders of Major Disciplines in Jiangxi Province (20182BCB22020), and the Central Funds Guiding the Local Science and Technology Development-Fundamental Research (YDZX2021005).

Data Availability Statement: Not applicable.

Conflicts of Interest: The authors declare no conflict of interest.

References

1. Wilheim, R.; Franz, B.; Heinrich, C. Hardening Cobalt-Nickel-Chromium-Iron Alloys. US2247643A, 1 July 1941.
2. Boegehold, A.L.; Hanink; Dean, K.; Webbere; Fred, J. Wrought high temperature alloy. US2860968A, 18 November 1958.
3. Keiser, D.D.; Brown, H.L. *Review of the Physical Metallurgy of Alloy 718*; Office of Scientific and Technical Information, U.S. Department of Energy: Washington, DC, USA, 1976. [CrossRef]
4. Reed, R.C. *The Superalloys: Fundamentals and Applications*; Cambridge University Press: Cambridge, UK, 2006.
5. Akca, E.; Gürsel, A. A Review on Superalloys and IN718 Nickel-Based INCONEL Superalloy. *Period. Eng. Nat. Sci. (PEN)* **2015**, *3*. [CrossRef]
6. Sharma, D.K.; Filipponi, M.; Schino, A.D.; Rossi, F.; Castaldi, J.P. Corrosion behaviour of high temperature fuel cells: Issues for materials selection. *Metalurgija* **2019**, *58*, 347–351.
7. Stornelli, G.; Gaggiotti, M.; Mancini, S.; Napoli, G.; Rocchi, C.; Tirasso, C.; Di Schino, A. Recrystallization and Grain Growth of AISI 904L Super-Austenitic Stainless Steel: A Multivariate Regression Approach. *Metals* **2022**, *12*, 200. [CrossRef]
8. Azarbarmas, M.; Aghaie-Khafri, M.; Cabrera, J.M.; Calvo, J. Microstructural evolution and constitutive equations of Inconel 718 alloy under quasi-static and quasi-dynamic conditions. *Mater Des.* **2016**, *94*, 28–38. [CrossRef]
9. Shi, X.; Duan, S.; Yang, W.; Guo, H.; Guo, J. Solidification and Segregation Behaviors of Superalloy IN718 at a Slow Cooling Rate. *Materials* **2018**, *11*, 2398. [CrossRef]
10. Thomas, A.; El-Wahabi, M.; Cabrera, J.M.; Prado, J.M. High temperature deformation of Inconel 718. *J. Mater. Process. Technol.* **2006**, *177*, 469–472. [CrossRef]
11. Brooks, J.W. Forging of superalloys. *Mater Des.* **2000**, *21*, 297–303. [CrossRef]
12. Lin, Y.C.; Wu, X.Y.; Chen, X.M.; Chen, J.; Wen, D.X.; Zhang, J.L.; Li, L.T. EBSD study of a hot deformed nickel-based superalloy. *J. Alloy. Compd.* **2015**, *640*, 101–113. [CrossRef]
13. Jonas, J.J. Dynamic recrystallization—Scientific curiosity or industrial tool? *Mater. Sci. Eng. A* **1994**, *184*, 155–165. [CrossRef]
14. Park, N.K.; Kim, J.H.; Yeom, J.T. Recrystallization and grain growth during alloy 718 processing. *Mater. Sci. Forum* **2007**, *539–543*, 3094–3099. [CrossRef]
15. Chen, X.-C.; Shi, C.-B.; Guo, H.-J.; Wang, F.; Ren, H.; Feng, D. Investigation of Oxide Inclusions and Primary Carbonitrides in Inconel 718 Superalloy Refined through Electroslag Remelting Process. *Met. Mater. Trans. B* **2012**, *43*, 1596–1607. [CrossRef]
16. Yang, S.-f.; Yang, S.-l.; Qu, J.-l.; Du, J.-h.; Gu, Y.; Zhao, P.; Wang, N. Inclusions in wrought superalloys: A review. *J. Iron Steel Res. Int.* **2021**, *28*, 921–937. [CrossRef]
17. Liao, L.; Li, J.; Zhao, Z.; Xu, F.; Zhang, W. Precipitation and phase transformation behavior during high-temperature aging of a cobalt modified Fe-24Cr-(22-x)Ni-7Mo-xCo superaustenitic stainless steel. *J. Mater. Sci.* **2022**, *57*, 4771–4788. [CrossRef]
18. Manikandan, S.G.K.; Sivakumar, D.; Kamaraj, M. (Eds.) 1-Physical metallurgy of alloy 718. In *Welding the Inconel 718 Superalloy*; Elsevier: Amsterdam, The Netherlands, 2019; pp. 1–19.

19. Bhowal, P.R.; Wusatowska-Sarnek, A.M. Carbides and their influence on notched low cycle fatigue behavior of fine-grained IN718 gas turbine disk material. In Proceedings of the 6th International Symposium on Superalloys 718, 625, 706 and Derivatives, Pittsburgh, PA, USA, 2–5 October 2005; pp. 341–349.
20. Araujo, L.S.; Guimarães, A.V.; Siqueira, M.C.; Mendes, M.C.; Mallet, L.; Silva dos Santos, D.; Henrique de Almeida, L. The influence of the processing route on the fragmentation of (Nb,Ti)C stringers and its role on mechanical properties and hydrogen embrittlement of nickel based alloy 718. *Int. J. Hydrogen Energy* **2021**, *46*, 16164–16178. [CrossRef]
21. Sohrabi, M.J.; Mirzadeh, H.; Rafiei, M. Solidification behavior and Laves phase dissolution during homogenization heat treatment of Inconel 718 superalloy. *Vacuum* **2018**, *154*, 235–243. [CrossRef]
22. Chen, K.; Rui, S.-Y.; Wang, F.; Dong, J.-X.; Yao, Z.-H. Microstructure and homogenization process of as-cast GH4169D alloy for novel turbine disk. *Int. J. Min. Met. Mater.* **2019**, *26*, 889–900. [CrossRef]
23. Miao, Z.J.; Shan, A.D.; Wu, Y.B.; Lu, J.; Hu, Y.; Liu, J.L.; Song, H.W. Effects of P and B addition on as-cast microstructure and homogenization parameter of Inconel 718 alloy. *Trans. Nonferrous Met. Soc. China* **2012**, *22*, 318–323. [CrossRef]
24. Moretti, M.A.; Dalai, B.; Åkerström, P.; Arvieu, C.; Jacquin, D.; Lacoste, E.; Lindgren, L.-E. High Strain Rate Deformation Behavior and Recrystallization of Alloy 718. *Metall. Mater. Trans. A* **2021**, *52*, 5243–5257. [CrossRef]
25. Vander Voort, G.; Manilova, E. Metallographic Techniques for Superalloys. *Microsc Microanal* **2004**, *10*, 690–691. [CrossRef]
26. Radavich, J.F. Electron metallography of alloy 718. In Proceedings of the International Symposium on Superalloys 718, 625, 706 and Various Derivatives, Pittsburgh, PA, USA, 2–5 October 2005; pp. 17–26.
27. Mitchell, A. The precipitation of primary carbides in IN718 and its relation to solidification conditions. In Proceedings of the 6th International Symposium on Superalloys 718, 625, 706 and Derivatives, Pittsburgh, PA, USA, 2–5 October 2005; pp. 299–310.
28. Mitchell, A. Primary Carbides in Alloy 718. In Proceedings of the 7th International Symposium on Superalloy 718 & Derivatives, Pittsburgh, PA, USA, 10–15 October 2010; Volume 1, pp. 161–167.
29. Sundararaman, M.; Mukhopadhyay, P.; Banerjee, S. Some aspects of the precipitation of metastable intermetallic phases in INCONEL 718. *Metall. Trans. A* **1992**, *23*, 2015–2028. [CrossRef]
30. Zenk, C.H.; Feng, L.; McAllister, D.; Wang, Y.; Mills, M.J. Shearing mechanisms of co-precipitates in IN718. *Acta Mater.* **2021**, *220*, 117305. [CrossRef]
31. Phillips, P.J.; McAllister, D.; Gao, Y.; Lv, D.; Williams, R.E.A.; Peterson, B.; Wang, Y.; Mills, M.J. Nano γ'/γ'' composite precipitates in Alloy 718. *Appl. Phys. Lett.* **2012**, *100*, 211913. [CrossRef]
32. Theska, F.; Stanojevic, A.; Oberwinkler, B.; Ringer, S.P.; Primig, S. On conventional versus direct ageing of Alloy 718. *Acta Mater.* **2018**, *156*, 116–124. [CrossRef]
33. Huang, K.; Logé, R.E. A review of dynamic recrystallization phenomena in metallic materials. *Mater Des.* **2016**, *111*, 548–574. [CrossRef]
34. Zhang, F.X.; Liu, D.; Yang, Y.H.; Liu, C.X.; Zhang, Z.; Wang, H.; Wang, J.G. Investigation on the meta-dynamic recrystallization behavior of Inconel 718 superalloy in the presence of delta phase through a modified cellular automaton model. *J. Alloy. Compd.* **2020**, *817*, 152773. [CrossRef]
35. Touazine, H.; Chadha, K.; Jahazi, M.; Bocher, P. Characterization of Subsurface Microstructural Alterations Induced by Hard Turning of Inconel 718. *J. Mater. Eng. Perform.* **2019**, *28*, 7016–7024. [CrossRef]
36. Kotan, H.; Darling, K.A.; Luckenbaugh, T. High Temperature Mechanical Properties and Microstructures of Thermally Stabilized Fe-Based Alloys Synthesized by Mechanical Alloying Followed by Hot Extrusion. *Met. Mater. Int.* **2021**, *27*, 1790–1797. [CrossRef]
37. Humphreys, J.; Rohrer, G.S.; Rollett, A. Chapter 13—Hot Deformation and Dynamic Restoration. In *Recrystallization and Related Annealing Phenomena*, 3rd ed.; Humphreys, J., Rohrer, G.S., Rollett, A., Eds.; Elsevier: Oxford, UK, 2017; pp. 469–508.
38. Wang, Y.; Shao, W.Z.; Zhen, L.; Lin, L.; Cui, Y.X. Investigation on dynamic recrystallization behavior in hot deformed superalloy Inconel 718. In Proceedings of the Beijing International Materials Week, Beijing, China, 25–30 June 2006; pp. 1297–1300.
39. Schuh, C.A.; Lu, K. Stability of nanocrystalline metals: The role of grain-boundary chemistry and structure. *MRS Bull.* **2021**, *46*, 225–235. [CrossRef]